



UNIVERSITÀ DI PARMA

ARCHIVIO DELLA RICERCA

University of Parma Research Repository

Flexible porous molecular materials responsive to CO₂, CH₄ and Xe stimuli

This is the peer reviewed version of the following article:

Original

Flexible porous molecular materials responsive to CO₂, CH₄ and Xe stimuli / Marchio, L; Mazzeo, PAOLO PIO. - In: JOURNAL OF MATERIALS CHEMISTRY. A. - ISSN 2050-7488. - 6:29(2018), pp. 14231-14239. [10.1039/c8ta02211a]

Availability:

This version is available at: 11381/2850609 since: 2021-10-19T10:49:09Z

Publisher:

Royal Society of Chemistry

Published

DOI:10.1039/c8ta02211a

Terms of use:

Anyone can freely access the full text of works made available as "Open Access". Works made available

Publisher copyright

note finali coverpage

(Article begins on next page)

This document is the Accepted Manuscript version of a Published Work that appeared
in final form in
Journal of Materials Chemistry A,
copyright © The Royal Society of Chemistry after peer review and technical editing by
the publisher.

To access the final edited and published work see

<https://doi.org/10.1039/C8TA02211A>



Flexible Porous Molecular Materials Responsive to CO₂, CH₄ and Xe Stimuli

Irene Bassanetti,^a Silvia Bracco,^a Angiolina Comotti,^a Mattia Negroni,^a Charl Bezuidenhout,^a Stefano Canossa,^b Paolo Pio Mazzeo,^b Luciano Marchio^{*,b} and Piero Sozzani^{*,a}

Received 00th January 20xx,
Accepted 00th January 20xx

DOI: 10.1039/x0xx00000x

www.rsc.org/

In the search for flexible molecular crystals endowed with porosity, we achieved the fabrication of expandable crystalline prototypal structures, which allow for the absorption of gases, without modifying the crystal architecture. The design brings together highly symmetrical tetrahedral elements to construct swellable porous adamantoid frameworks through co-operation of 8 surrounding hydrogen bonds mounted on conformationally flexible groups. The flexibility of the porous crystals manifests itself in response to stimuli of selected gases, which promote reversible conformational changes, inducing a breath to the molecular building. The backbone of the reticular construction is based on the formation of carboxylic dimers, which project outwards from the tetrahedral molecular core to consolidate the 3D framework. The contact with proper gases such as CO₂, Xe and hexane triggers the 56-70% enlargement of channel cross-section. The accommodation of CO₂ and Xe in the channel chambers was revealed by synchrotron-light X-ray diffraction, combined with Molecular Dynamics and DFT theoretical calculations. Rare experimental observations of xenon dynamics, while Xe diffuses along the channels and experiences different chamber orientations in the crystal, were gathered by analysing ¹²⁹Xe NMR chemical shift anisotropy profiles, which encode the shape and orientation of each visited cavity along the channel. Jump rate and activation energy experienced by exploring Xe atoms in their diffusional path were uniquely established. Nitrogen showed low affinity to the matrix and was unable to enlarge the pores, thus it is excluded from the restrictive pores of the empty crystal. Given the prerogatives of the molecular crystals, it is possible to outline some advantageous aspects, such as simple design, easy self-assembly, solubility, reversible gas uptake and absence of metal ions: they can thus be considered for eco-friendly gas capture and separation.

Introduction

A great attention has been paid during the last years to the capture and release of gases by the aid of nanoporous solids. The design of new-generation porous materials enables innovative technologies for removal of green-house gases from exhaust fumes, their recycle and transformation.¹ Among other versatile materials, such as hybrid frameworks, most promising are fully-organic porous structures whose architectures can be fabricated by discrete molecules.² In contrast to metal organic and covalent organic frameworks which are sustained by high-energy bonds, molecular materials are self-assembled by soft and reversible interactions and express the highest modularity, processability and easy crystal formation, enabling the fabrication of large single crystals.

In this emerging class of materials, the presence of cavities may be intrinsic to the molecules themselves, alternatively porous molecular crystals with porosity extrinsic to the constituting molecules may generate channels, chambers and galleries by assembling the molecules into a low-density framework.³ The interest for single-component permanently porous molecular crystals with extrinsic porosity have emerged in two decades and the number of examples reported so far is still limited.⁴

Porous solids, produced by soft non-covalent interactions, are challenging for their simple design, flexibility and easy pore regeneration. The versatility of the organic synthesis enables a facile modulation of the interactions, which range from soft van der Waals and π - π interactions to hydrogen bond formation.^{5,6} These features cooperate together with shape factors, including symmetry, for tuning effectively pore size and dimension in the architecture.

Multiple (≥ 3) complementary functional groups attached to the same core promote the formation of frameworks by functional group recognition. Hydrogen bonds (HBs) represent a constant motif in the formation of porous molecular structures, as shown for instance by the use of aminoacids (dipeptides), sulfonate/ammonium (organic salts), diamino groups (HOFs) and carboxylic/pyridil groups. (SOFs).^{4f,7,8}

For what regards shape and symmetry factors, three or more functional groups protruding radially produce directional interactions developed in space, depicting a molecular structure

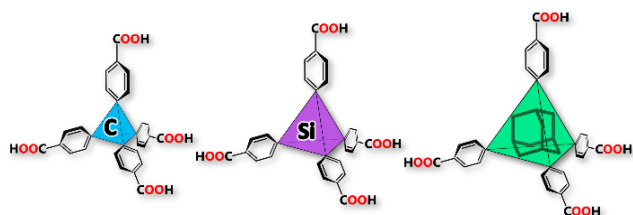
^a Department of Materials Science, University of Milano Bicocca, Via R. Cozzi 55, 20125 Milan, Italy

^b Department SCVSA, University of Parma, via delle Scienze 17/a, 43124 Parma, Italy.

† Footnotes relating to the title and/or authors should appear here.

Electronic Supplementary Information (ESI) available: Synthesis and preparation of materials, SCXRD, PXRD, IR, TGA, DSC, results of density functional theory calculations, GCMC simulations, Langmuir-Freundlich isotherm model, fitting, isosteric heat of adsorption calculation (PDF). Crystallographic file of porous TCF-1, TCF-1/guest, TCF-1/CO₂, TCF-1/Xe, close-packed TCF-1, TCF-2, TCF-3 (CIF).

favourable to the formation of porosity. To achieve this, the highly-symmetric tetrahedral node (S_4 point group) seems a valid primary element that constitutes a kind of prototype. Tetrahedral struts⁹ have proved successful in sustaining permanently porous materials. Tetraphenylmethane, tetraphenylsilane and tetraphenyladamantane, as connectors, have attracted much attention. Indeed, porous aromatic frameworks PAF-1 and PAF-3 wherein a tetrahedral unit is connected by carbon-carbon bonds, and covalent organic frameworks COF-102 and COF-103 forming a tetrahedral based boroxane network yielded paramount surface areas.¹⁰ However, so far the examples of molecular crystals based on tetracarboxylic acids such as methanetetraabzoic acid MTB and silanetetraabzoic acid STB were described to form closely-packed architectures,¹¹ although such tetracarboxylic ligands were often used for the synthesis of MOFs.¹² Herein we have proved the generation of porous diamondoid 3D-architectures (tetracarboxylic frameworks TCFs) sustained by tetrahedral building blocks (Scheme 1) that are connected by double H-bonding between two interacting carboxylic groups. The porous structure showed empty channels with cross-sections which expand up to 70% upon exposure to gases and vapors even at low pressures. The remarkable structure breathing is a rare instance of intrinsic gymnastic of the molecular elements in crystal flexibility: in fact, the expansion is obtained by the concerted conformational change of the benzoic units about the tetrahedral carbon.



Scheme 1. Chemical structures and geometries of MTB, STB and ATB building blocks, yielding TCF-1, TCF-2 and TCF-3, respectively.

The porous TCFs frameworks reversibly absorbed relevant gases such as CO_2 , CH_4 , xenon as well as hexane vapours. The crystal structures of the porous frameworks pressurized with CO_2 and Xe were solved by synchrotron-light single-crystal XRD analysis, highlighting gas preferred location. These results showed the changes in the dominant interactions with respect to the empty-pore arrangement. DFT calculations, Molecular Dynamics and Grand Canonical Monte Carlo simulations singled out specific gas-crystal interactions. Moreover, ^{129}Xe NMR could highlight the unconventional dynamics of gas atoms, which receive the imprinting of chamber orientations along the channels, since Xe tensor components reorient according to the symmetry of explored cavities. The anisotropic line-shape analysis provided the rates at variable temperature and the activation energy of the jumps from one site to the next. Collectively, we have realized porous molecular crystals based on hydrogen bonding containing expandable channels which can be easily switched upon exposure to gases and vapours and the dynamics of the diffused gases inside them.

Results and discussion

The tetracarboxylic-based frameworks (TCF) were obtained by crystallization of methanetetraabzoic acid MTB, silanetetraabzoic acid STB or adamantanetetraabzoic acid ATB in hexane/THF (TCF-1, TCF-2 and TCF-3, respectively). Their IR, TGA and DSC characterizations are reported in Figures S1-S5. Crystals suitable for single crystal XRD are obtained stratifying hexane over a solution of MTB, STB and ATB in THF (Table S1). The MTB forms an organic network TCF-1 with solvent molecules (space group $P4_2/n$) and is endowed with an extensive H-bond network. The TCF-1/guest was transformed into a porous framework by removal of the guest under mild conditions (vacuum of 10^{-2} mbar and slow heating from room temperature to 50°C) (Figure 1).

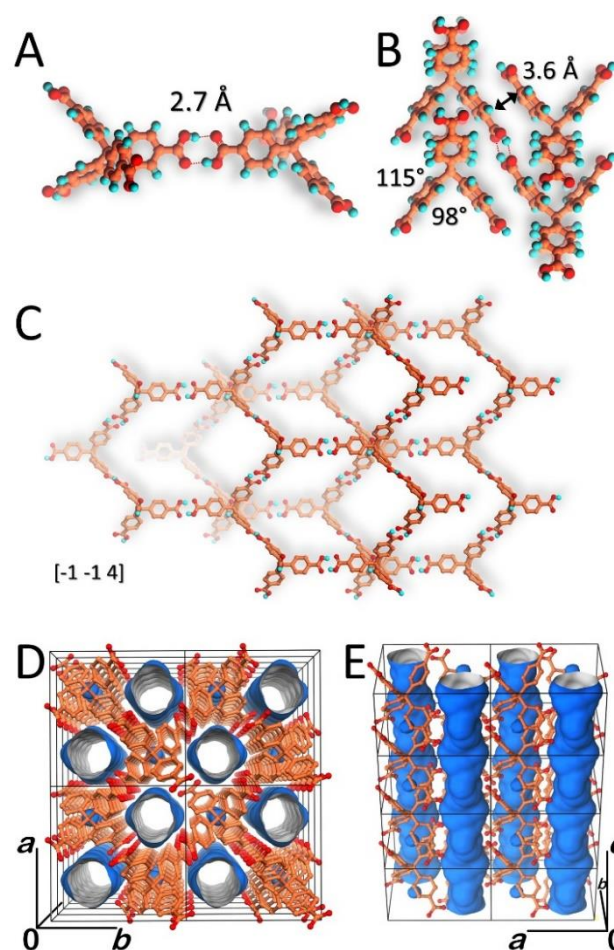


Figure 1. Molecular structure and crystal packing of the porous TCF-1 compound. A) Hydrogen-bonded dimer. B) Packings of supramolecular pillars. C) Single diamondoid HBS network. D and E) Crystal structure of the porous TCF-1 highlighting the empty channels in light blue, as viewed along and perpendicular to the c -axis. Distances are reported in Å.

The transformation was followed by *in situ* PXRD and the porous molecular structure was determined by Rietveld refinement (Figures S6-S7 and Table S2). The porous TCF-1 exhibits a diamondoid structure, wherein the quaternary carbon atoms, located on 4-fold rotoinversion crystallographic axis, play the

role of the nodes. A slight deviation from the ideal tetrahedral molecular geometry is apparent, since two C-O-C angles at the central carbon are 115° and 98°. Importantly, each molecule is connected to its four neighbours through eight H-bonds, provided by carboxyl dimers formation (Figure 1). The distance between the hydrogen bonded oxygen atoms is as short as 2.7 Å, as confirmed by high field fast-MAS ^1H NMR spectrum which exhibits a downfield chemical shift at 13.0 ppm for the carboxylic signals that corresponds to a distance of 2.6-2.7 Å (Figure S8).¹³ The supramolecular interactions exchanged by the tetra-functional molecular building-blocks are systematically coupled to construct an expanded diamondoid network (Figure 1C and S9). Each network is associated to the next by close contact interactions between the positively-charged carboxylic carbon and the π -phenyl groups (distance of 3.6 Å), further stabilizing the framework (Figure 1B). The molecular assembly leads to a porous framework which contains channels running parallel to the crystallographic c -axis and yielding a pore volume of 264 Å³/cell (as estimated by a sphere of 1.2 Å). The channel architecture consists of communicating cavities aligned along the c -axis. The cavities exhibit elliptical cross-sections (5.5×2.9 Å²) whose major axes are alternatively rotated by 90°. ^{13}C MAS NMR spectrum showed the guest absence in the channels (Figure S10). The flexibility of the architecture and the channel expansion upon gas adsorption will be demonstrated later. Interestingly, a thermal treatment in the 110-140 °C range of the empty structure triggers a phase transformation to the close-packed structure (Figure S11). The heat release for the formation of the non-porous form is accounted for by the more efficient packing. In the new phase (space group $I-4$), the torsion angle of the benzoic-unit plane about the $\text{Csp}^2\text{-Csp}^3$ of the tetrahedral unit is significantly rotated by 30° with respect to the porous framework (Figure S12). Notably, instead of carboxylic dimers, clusters of four carboxylic groups held together by four weaker hydrogen bonds are formed. The channel-like architecture recovers after wetting of the close-packed form with THF/hexane at room temperature and drying (Figures S10 and S13).

CO₂ adsorption and its arrangement in the structure

The permanent porosity of the TCF-1 was demonstrated by the CO₂ isotherm at 195 K, which shows a Langmuir type profile typical of a microporous structure. Figure 2 shows the experimental isotherm along with the GCMC predicted uptake. The porous TCF-1 can adsorb 96.8 cm³/g⁻¹ (4.3 mmol g⁻¹, i.e. 19.0 wt%), exceeding a number of materials based on stronger bonds, such as SNU-15: a Co²⁺ MOF,^{12c} which is constructed with the same tetrahedral building block (MTB⁴⁻) through coordination bonds. CO₂ adsorption isotherms collected up to 10 bar at 298 K and 273 K reach 72.3 and 76.6 cm³ g⁻¹ (STP), respectively.

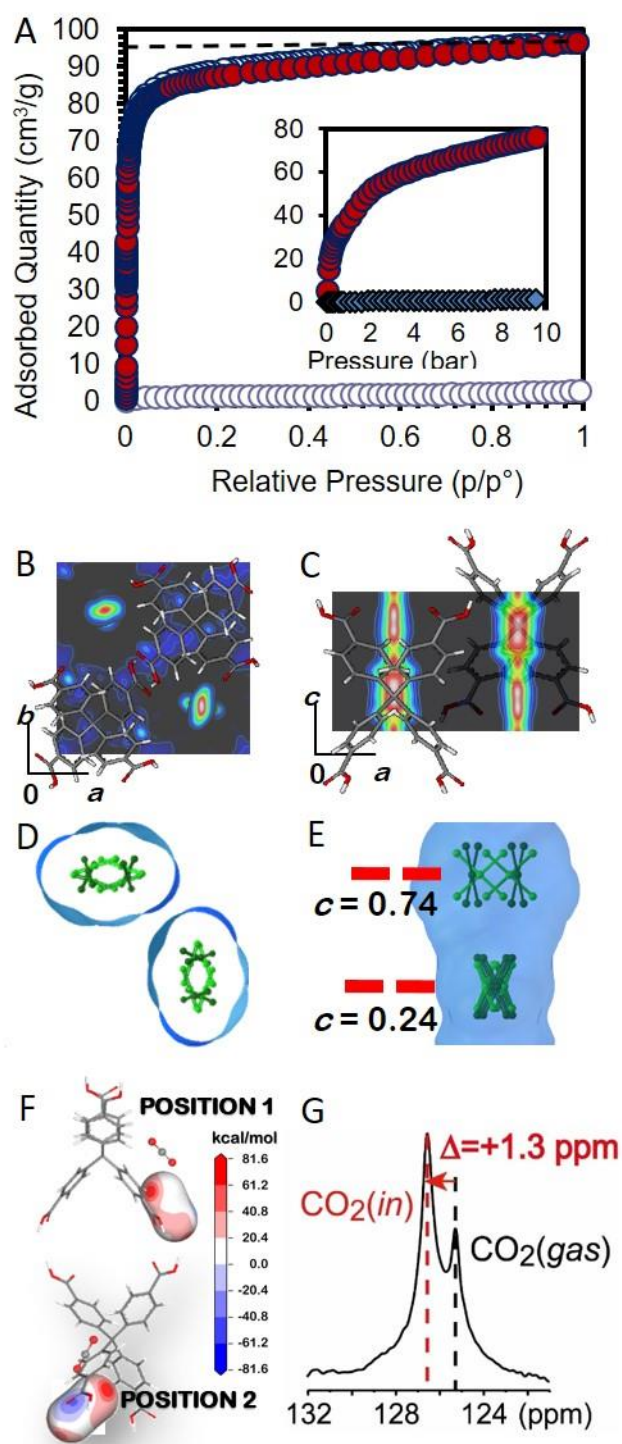


Figure 2. A) CO₂ isotherms collected at 195K on porous TCF-1 (adsorption: red circles, desorption: white circles) and its compacted form (adsorption: blue circles). In the inset the CO₂ and N₂ adsorption isotherms (red circles and blue diamonds, respectively) at 273 K and up to 10 bar. The dashed line indicates the maximum loading, as calculated by GCMC simulation of the CO₂ isotherm at 195 K. B and C) Electron density difference map ($F_0 - F_2$) for CO₂ loaded TCF-1 as viewed perpendicular to and along the c -axis, respectively. D and E) Simulated positions of CO₂ molecules within the channels of TCF-1 as viewed perpendicular to and along the c -axis, respectively. F) The molecular electrostatic potential of the TCF-1 host molecules and surrounding CO₂ molecules. Red indicates the positive potentials and blue negative potentials as shown by the scale bar. G) ^{13}C MAS NMR spectrum of TCF-1 sample loaded with ^{13}C -enriched CO₂.

It is worth noting that under the mild conditions of 1 bar and 273 K (Figure S14) TCF-1 adsorbs $40 \text{ cm}^3 \text{ g}^{-1}$ of CO_2 (1.76 mmol g^{-1} and 7.7 wt%), overcoming a few prominent porous molecular and metal-organic frameworks^{8b,14} and many covalent-based materials as, in particular, COF-102^{10f} and PAF-1,¹⁵ although their surface areas are markedly higher, giving credit to the fact that crystals with narrow channels are performant absorbers at low pressures.¹⁵ The isosteric heat of adsorption (Q_{st}) was calculated from CO_2 adsorption isotherms collected at distinct temperatures using Van't Hoff equation (Figure S15). At low coverage, the Q_{st} reaches 33 kJ mol^{-1} . This comparatively high value suggests multiple interactions installed simultaneously by the CO_2 molecule in the narrow channel.^{4a,4e,8c,16} Contrarily, N_2 adsorption is negligible likely because the pores in the empty structure are too narrow and the low affinity does not allow to open up the channels, therefore the CO_2/N_2 selectivity is higher than a few hundreds at 273K.

The crystal structure of TCF-1 loaded with CO_2 was solved by single crystal X-ray diffraction analysis, exploiting a synchrotron radiation source (Figure 2). Data collections were performed at 220 K showing the channel-like structure (space group $P4_2/n$), as already observed in the empty structure. The unit cell parameters are enlarged to $a=b=13.11 \text{ \AA}$ and $c=8.08 \text{ \AA}$ with a significant expansion of the channel cross-section to $6.2 \times 4.0 \text{ \AA}^2$. Thus, the cross-section area increases up to 56% with respect to that of the empty structure, showing the breathing of the porous framework upon loading.

The refinement of the residual electron density within the channels of 80 electrons per cell in CO_2 -loaded TCF-1, showed the presence of about 4 CO_2 molecules per unit cell, i.e. one per cage (Figure S16). The amount of CO_2 observed by single crystal XRD is in agreement with the saturation value of CO_2 isotherm at 195 K (4.3 CO_2 molecules per unit cell). Using electron density difference maps, it was possible to determine CO_2 distribution profiles within the cavities (Figure 2B and C). However, the orientation and interactions of CO_2 molecules in the channels was achieved by computational methods. A combination of Grand Canonical Monte Carlo simulation (GCMC) for CO_2 sorption, molecular dynamics simulation and DFT calculations, yielded prevailing CO_2 arrangements in the cavities, in agreement with the XRD electron density distribution (Figure 2D and E).

The prevailing configuration along the channel, with about 80% probability (configuration 1), according to the Boltzmann distribution at 220 K, reveals two distinct CO_2 orientations (Figure S17), with CO_2 main axis tilted by 30° and 50° with respect to the c -axis (position 1 and 2, respectively), that are correlated and alternate along the channels due to guest-guest steric exclusion. The host- CO_2 interaction energies for CO_2 positions 1 and 2 are $-26.8 \text{ kJ mol}^{-1}$ and $-26.1 \text{ kJ mol}^{-1}$ respectively while the CO_2 - CO_2 interaction energy is significantly lower (-6.0 kJ mol^{-1}). Furthermore, molecular electrostatic maps were calculated to explore the nature of these interactions. The electrostatic potential was calculated using the host and guest molecules within immediate proximity of the target CO_2 molecule (i.e. position 1 and 2).¹⁷ This electrostatic potential is then mapped onto an outer electron

density contour of the designated CO_2 molecules (Figure 2F). It is evident that the strongest electrostatic interactions occur between the host aromatic hydrogens and the oxygen atoms of CO_2 (red areas of the molecular electrostatic map), accounting for the occurrence of hydrogen bonds. The CO_2 - CO_2 and host- CO_2 electrostatic potentials mirror the calculated interaction energies. Additionally, areas of negative potential (weaker than the positive potentials) are located on the carbon atoms of the CO_2 molecules, further stabilizing CO_2 in position 2 within the channels.

^{13}C MAS NMR spectrum confirmed this arrangement and provided further details: actually, ^{13}C enriched CO_2 pressurized with the porous crystals showed two distinct resonances (Figure 2G): one upfield ($\delta=125.3 \text{ ppm}$) for the gas phase and another downfield ($\delta=126.6 \text{ ppm}$), which pertains to the CO_2 diffused into the porous crystals. The relative shift of $\Delta(\delta\text{CO}_{2in} - \delta\text{CO}_{2out}) = +1.3 \text{ ppm}$ indicates that CO_2 carbons sit approximately in the plane of the p -phenylene rings within the deshielding region induced by the ring-current,¹⁸ consistently with the CO_2 arrangement favourable to the formation of C-H...O interactions,⁷ as depicted in Figure 2E.

Hydrocarbon and CH_4 adsorption

A particular feature of the porous TCF-1 is its ability to adsorb methane and hexane. The CH_4 isotherm collected at 195K shows an uptake of $43.7 \text{ cm}^3/\text{g}$ (Figure 3), suggesting that 2 CH_4 molecules per unit cell are adsorbed, consistent with the larger size of the CH_4 molecules than the CO_2 .

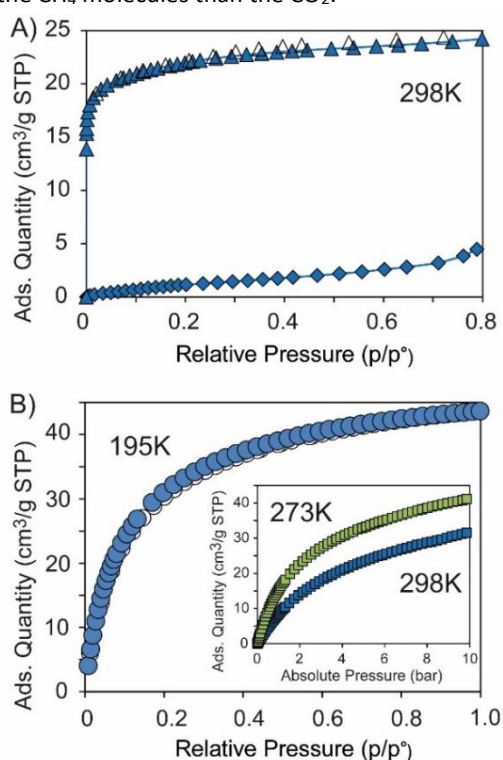


Figure 3. A) Hexane vapor adsorption isotherms collected at 298K on porous TCF-1 and its close-packed form (blue triangles and diamonds, respectively). B) CH_4 isotherms at 195 K (blue circles). In the inset, CH_4 isotherms at 273K and 298K (green and blue squares, respectively).

The isosteric heat of CH₄ adsorption (Q_{st}) as calculated from adsorption isotherms at distinct temperatures was 21 kJ/mol, and remains constant throughout the pressure range (Figures S18–S20). This value is higher than most MOFs¹⁹ thanks to the narrow cross section of the channel that enables multiple interactions with walls. In fact, evidences show that, at low coverage, the Q_{st} increases with decreasing pore size and surface area, explaining the good affinity of methane for TCF-1. In the case of hexane a Langmuir profile with virtually a full loading of hexane from the vapour phase is achieved already at low partial pressure 0.1 (15 torr) showing the great affinity towards this vapour (Figure 3). Considering the elongated hexane length of 12 Å in a narrow channel, the filling of the channels corresponds to 85% of the theoretical value. The process is fully reversible as shown by the desorption curve. These results indicate the efficiency of TCF-1 system for hydrocarbon capture.

From the single crystal XRD analysis, the TCF-1/hexane displays an expansion of the unit cell volume (5%) and of the a/b axes from 12.76 Å to 13.20 Å from empty to guest-containing TCF-1, respectively. In the TCF-1/hexane, the carboxylic dimer is preserved as the dominant interaction between adjacent molecules ($d_{O-O} = 2.63$ Å). Interestingly, the torsion angle of the benzoic-unit plane about the Csp²–Csp³ bond of the tetrahedral unit is rotated by 10°, showing the breathing of the structure upon absorption of the guest. The TCF-1/hexane exhibits expanded channels compared to the empty structure, with a cross section of 6.3×4.2 Å² which corresponds to an increased cross-section area of 66%.

Xe adsorption and dynamics

Porous TCF-1 can also adsorb efficiently Xe from the gas phase (Figure S21), thus, single crystals of porous TCF-1 were loaded with Xe (150 torr and 220K) and analysed by X-ray diffraction using synchrotron radiation. Interestingly, we observe a 6% volume expansion of the unit cell that still conserves both the channel-like architecture and the double hydrogen-bonded dimer between the carboxylic groups of the building blocks. The electron density difference map allowed us to accurately establish Xe location at each site along the channels with an occupation factor of 0.6 (Figure 4). The electron density on the x - y plane intersecting the center of the cavity exhibited an elongated shape, which mirrors the elliptical development of the cavity (Figure 4B). The direction of the elliptical main axis is alternatively rotated by 90° in each adjacent cavity along the c -axis. The cross-section is expanded to 6.4×4.2 Å² when Xe atoms are confined inside the cavities producing a cross-section area enlargement of 70%. The Xe atoms realize a tight fitting within the cavities: Xe is at van der Waals contact with the surrounding host atoms (Figure S22). Ab initio calculations of the interaction energies yielded a significantly strong Xe–Host interaction energy of -36.0 kJ mol⁻¹ and a Xe–Xe interaction energy of -2.6 kJ mol⁻¹ (Figure S23). The latter value is consistent with the dimer dissociation energy of -2.4 kJ mol⁻¹ reported in the literature.²⁰

Moreover, it was possible to determine the most probable Xe configurations within the crystal structure by molecular dynamics and ab initio calculations. A super-cell that consists of 5 unit-cells, yielding a channel with 10 sites occupied by 6 Xe atoms (according to the experimental occupation factor of 0.6), was used. The arrangement of Xe atoms in a chain realized the most energetically stable configuration, while the arrangements in shorter Xe sequences are characterized by higher energies (Figures S24–S29 and Table S3). By applying the Boltzmann distribution at 220 K to the energy levels of the distinct configurations, and taking into account their multiplicity, we determined that short Xe chains (dimers and trimers), randomly distributed along the channel file, prevail over longer sequences.

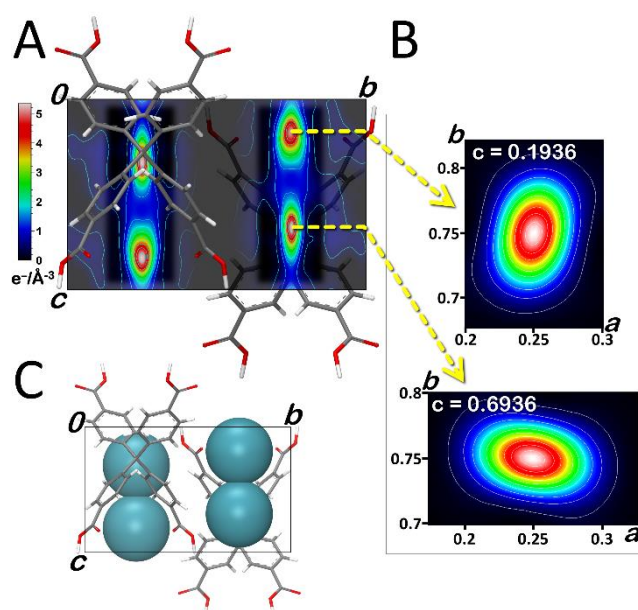


Figure 4. (A and B) Electron density difference map ($F_o - F_c$) for Xenon loaded TCF-1 as viewed perpendicular to and along the c -axis, respectively. (C) Crystal structure of Xenon loaded TCF-1. Modelled Xe atoms shown in space-filling representations and the host molecules in stick.

¹²⁹Xenon under natural abundance is an invaluable NMR probe to explore any accessible material cavity, and returns information on pore size and symmetry, as well as on diffusional behavior of xenon in the channels.²¹ ²⁹Xe NMR spectra were collected at variable temperature, after pressurizing xenon with the crystalline powder (9 bar at room temperature). In addition to the Xe-gas resonance at about 0 ppm, anisotropic signals in the 190–310 ppm range are generated by Xe atoms confined to the accessible pores. Such remarkably downfield chemical shift values and the anisotropic pattern, achieved here under high Xe loading,²² indicate the tight fit in the host sites, as well as confining interactions with other Xe atoms that explore the channel. Collectively the intriguing line-shape change with temperature (Figure 5A) was interpreted and simulated as the effect of thermally activated Xe-jumps to adjacent vacant cavities along the channel. This jump entails a 90° reorientation of the principal tensor components, which is dictated by the

orientation of cavities: actually, ^{129}Xe NMR anisotropy reports on the elliptical cross-section, whose orientation in the x - y plane is rotated by 90° in the next chamber along the channel (Figure 5B).

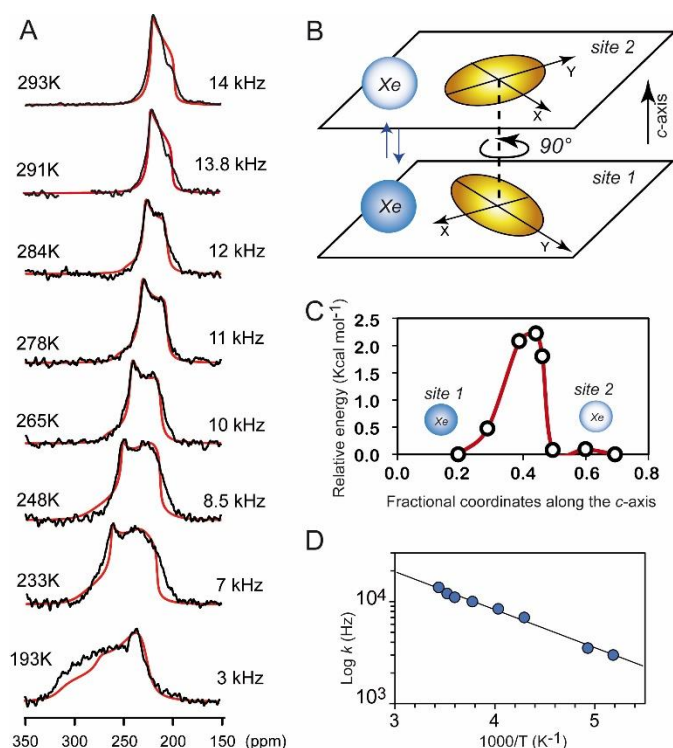


Figure 5. A) Variable temperature ^{129}Xe NMR spectra of TCF-1 loaded with Xe. The reorientational rates k are reported. B) Schematic representation of Xe jumps between two sites and the orientation of elliptical cross-section in two adjacent cavities. C) Energy profile for the trajectory of Xe from one cavity to the next by *ab initio* calculation applying the CASTEP transition state code. D) Arrhenius plot of experimental reorientational rates k versus the reciprocal of temperature.

As a consequence of diffusional motion, Xe dynamically explores the two site orientations and, if the exchange rates exceed the frequency difference between the principal tensor components, Xe perceives an averaged interaction. Actually, at room temperature the ^{129}Xe NMR spectrum is simulated by δ_{xx} and δ_{yy} orthogonal components averaged out by 90° jumps between sites with a fast exchange rate $> 2 \times 10^4$ Hz, that merge in the singularity at 243 ppm. Under these dynamic conditions, the channel is perceived by diffusing xenon, as a cylinder. In the regime of single-file diffusion, e.g. xenon atoms cannot bypass each other, Xe diffusion is restricted,²³ however, a few vacancies are enough to impart dynamics to the entire Xe population by a defect-propagation effect. By lowering the temperature, xenon atoms reside in a single elliptically-shaped cavity for a time comparable to or longer than the reciprocal of resonance separation, resulting in complex lineshapes due to the partial averaging among the main components of the tensor. Arrhenius plot provided an energy barrier of 1.8 kcal mol⁻¹ for the site jump, consistent with the value of the barrier height of Xe trajectory along channel axis (2.5 kcal mol⁻¹) as

calculated by *ab initio* calculation of Xe-shuttle moving from one site to another (Figures 5C and Table S4).

Expanded building blocks in TCF-2 and TCF-3 compounds

In an attempt to enlarge the channel dimensions in the crystal structure, compounds containing tetrahedral cores of silicon (STB) and adamantane (ATB) were chosen, instead of carbon, as building blocks. The framework TCF-2, as obtained by STB self-assembly, crystallizes in the tetragonal $I4_1cd$ space group (Figure 6). The asymmetric unit comprises 1.5 STB molecular units, indicated as Si1 and Si2 (the latter lying on a twofold axis). The constructive elements are held together by carboxylic acid twinning as above described. STB, endowed with longer Si-C bond distances in the 1.83-1.93 Å range, is not prone to assemble into the pillared arrangement as in TCF-1, but into an interpenetrated network containing cavities with a volume of 13165 Å³ that corresponds to 51% of the unit cell volume (estimated by PLATON) is formed. From an analysis of the residual electron density it is observed that the cavities are occupied by disordered solvent molecules.

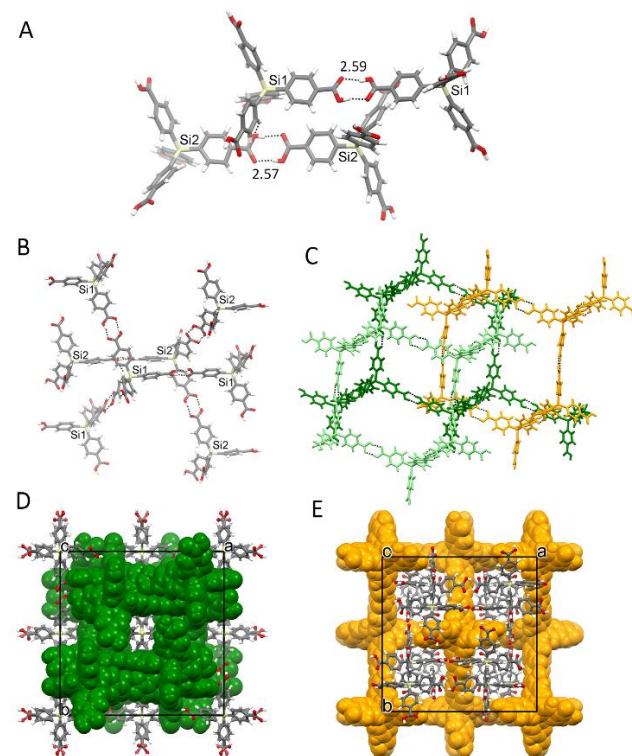


Figure 6. Molecular structure and crystal packing of TCF-2. Hydrogen bond dimers, distances are reported in Å (A); Expansion of the two independent molecules of the asymmetric unit (B); Interconnection of the diamondoid HB networks formed by TCF-2, in green, and Si2-containing system, in orange (C). Packing projected along the c axis of the networks formed by Si1-containing system, green, and by TCF-2 orange (D, E).

DSC studies, performed in the 25-200° C range, allow us to investigate the stability of the framework as a function of temperature (Figure S30). Notably, the guest-containing TCF-2 shows, in addition to the endothermic peak at 60°C due to guest solvent release, an exothermic peak at 163°C with an enthalpy value of $\Delta H=22$ J/g. A similar exotherm peak was observed in a sample of TCF-2, previously subjected to a thermal treatment at

100°C overnight, suggesting the formation of the porous structure that transforms into a more compact form above 160°C. Interestingly similar exotherm peaks with comparable enthalpy values were measured in porous molecular materials, confirming the retention of the light framework upon guest removal.^{4a} The porosity of the material was confirmed by the CO₂ adsorption isotherm at 195K (Figure S31).

The framework with the adamantane core TCF-3 crystallizes in the tetragonal *P4/n* space group (Figure S32). The asymmetric unit comprises part of the adamantane moiety linked to an aromatic ring and the solvent molecules. One is located in the channel-like cavities while the other plays a structural role by linking together two carboxylic functions (Figure S33). Interestingly, the presence of the THF molecules disrupt the formation of the carboxylic dimer and promote the formation of a side-to-side interaction between the peripheral arms of ATB. The molecules form pillars that interact with four symmetry related pillars by means of the THF-mediated interaction. This structural arrangement leads to the formation of a channel-like cavity, which is occupied by disordered THF molecules.

Conclusions

We successfully explored the possibility of constructing porous diamondoid molecular architectures by the sole use of highly symmetric tetrahedral building blocks. The dimer formation between carboxylic functions was exploited to fabricate porous molecular frameworks by self-assembly of the tetracarboxylic-based precursors. This was made possible by the energetics of the carboxylic dimerization, involving the formation of two hydrogen bondings and the favorable features of the high symmetry building blocks. The coupling of the 4 carboxylic groups involved the formation of 8 hydrogen bonds in a first molecular sphere and the exponential increase of the number of hydrogen bonds in the next spheres for the formation of a robust yet flexible 3D network. The ultra-microporous nature of the frameworks featured specific sorptive capacities for monoatomic gas (Xe) and molecules, such as CO₂ and CH₄, relevant gases for environment and energy reasons. Single-crystal synchrotron-radiation XRD analysis could highlight by the electron density distribution, the location of CO₂ and Xe gases sitting in the channel sites. Moreover, the fast dynamics of Xe atoms in the nanochannels with a jump rate of 14 kHz at room temperature and an energy barrier as low as 1.7 kcal mol⁻¹ were measured by ¹²⁹Xe NMR anisotropic lineshape change versus temperature. Thermal stimuli trigger the transformation from the porous to a close-packed form, impermeable to gases and vapors, viceversa the channel-like structure can be easily regenerated by treatment with a liquid guest.

These results enforce the idea that the use of simple molecules endowed with suitable symmetry promotes the generation of the exquisite architectures. The symmetrical shape of the molecules, whose branches rigidly expand in 3D, produces not only clathrates, but originates molecular frameworks with permanent porosity and guest-responsive pore flexibility. Porous molecular solids are of great interest since they are

versatile, soluble and switchable. The above conclusion reinforces the idea that unusual crystalline forms endowed with new functions and properties are still to be searched among the simple organic molecules. The open framework is especially prone to accept gases and volatile hydrocarbons, enabling the preparation of innovative materials for gas capture and separation.

Conflicts of interest

There are no conflicts to declare.

Acknowledgements

A. C. would like to thank MIUR-PRIN 2016-NAZ-104, Cariplo Foundation 2016 BALANCE and INSTM Consortium/Lombardy Region 14-2016 for fundings. We thank Dr. Nicola Demistri (Elettra Synchrotron Facility) for technical advice. Chiesi Farmaceutici Spa is acknowledged for their support in the acquisition of the single crystal X-ray diffraction equipment.

Notes and references

- (a) A. Schoedel, Z. Li and O. M. Yaghi, *Nature Energy*, 2016, **1**, 1-13; (b) H. C. Zhou and S. Kitagawa, *Chem. Soc. Rev.*, 2014, **43**, 5415-5418; (c) S. Das, P. Heasman, T. Ben and S. Qiu, *Chem. Rev.*, 2017, **117**, 1515-1563; (d) Z. Zhang and M. J. Zaworotko, *Chem. Soc. Rev.*, 2014, **43**, 5444-5455; (e) K. Adil, Y. Belmabkhout, R. S. Pillai, A. Cadiau, P. M. Bhatt, A. H. Assen, G. Maurin and M. Eddaoudi, *Chem. Soc. Rev.*, 2017, **46**, 3402-3430.
- (a) N. B. J. McKeown, *J. Mater. Chem.*, 2010, **20**, 10588-10597; (b) J. R. Holst, A. Trewin and A. J. Cooper, *Nature Chem.*, 2010, **2**, 915-920.
- J. Lu and R. Cao, *Angew. Chem. Int. Ed.*, 2016, **55**, 9474-9480.
- (a) P. Sozzani, S. Bracco, A. Comotti, L. Ferretti and R. Simonutti, *Angew. Chem. Int. Ed.*, 2005, **44**, 1816-1820; (b) S. J. Dalgarno, P. K. Thallapally, L. J. Barbour and J. L. Atwood, *Chem. Soc. Rev.*, 2007, **36**, 236-245; (c) K. J. Msayib, D. Book, P. M. Budd, N. Chaukura, K. D. M. Harris, M. Helliwell, S. Tedds, A. Walton, J. E. Warren, M. Xu and N. B. McKeown, *Angew. Chem. Int. Ed.*, 2009, **48**, 3273-3277; (d) A. Comotti, S. Bracco, G. Distefano and P. Sozzani, *Chem. Comm.*, 2009, 284-286; (e) H. Kim, Y. Kim, M. Yoon, S. Lim, S. M. Park, G. Seo and K. Kim, *J. Am. Chem. Soc.*, 2010, **132**, 12200-12202; (f) M. Mastalerz, M. W. Schneider, I. M. Oppel and O. Presly, *Angew. Chem. Int. Ed.*, 2011, **50**, 1046-1051; (g) V. N. Yadav, A. Comotti, P. Sozzani, S. Bracco, S.; T. Bonge-Hansen, M. Hennem and C. H. Gorbitz, *Angew. Chem. Int. Ed.*, 2015, **54**, 15684-15688; (h) M. Baroncini, S. D'Agostino, G. Bergamini, P. Ceroni, A. Comotti, P. Sozzani, I. Bassanetti, F. Grepioni, T. M. Hernandez, S. Silvi, M. Venturi and A. Credi, *Nature Chem.*, 2015, **7**, 634-640.
- (a) C. B. Varshnev, J. R. G. Sander, T. Friscic, L. R. MacGillivray, in *Supramolecular Chemistry: From Molecules to Nanomaterials*, (eds.: J. W. Steed, P. A. Gale), Wiley-VCH, Weinheim, 2012, pp. 9-24. (b) K. Raatikainen and K. Rissanen, *Chem. Sci.* 2012, **3**, 1235-1239; (c) D. Holden, S. Y. Chong, I. Chen, K. E. Jeffs, T. Hasell and A. I. Cooper, *Chem. Sci.*, 2016, **7**, 4875-4879.
- G. R. Desiraju, T. Steiner, *The Weak Hydrogen Bond in Structural Chemistry and Biology*, Oxford University Press, Oxford, 1999.

- 7 (a) C. H. Görbiz, *Chem. Eur. J.*, 2007, **13**, 1022-1031; (b) A. Comotti, S. Bracco, A. Yamamoto, M. Beretta, T. Hirukawa, N. Tohnai, M. Miyata and P. Sozzani, *J. Am. Chem. Soc.*, 2014, **136**, 618-621; (c) Y. Liu, C. Hu, A. Comotti and M. D. Ward, *Science*, 2011, **333**, 436-440; (d) S. A. Dalrymple and G. K. H. Shimizu, *J. Am. Chem. Soc.*, 2007, **129**, 12114-12116; (e) J. Lü, C. Perez-Krap, M. Suyetin, N. H. Alsmail, Y. Yan, S. Yang, W. Lewis, E. Bichoutskaia, C. C. Tang, A. J. Blake, R. Cao and M. Schröder, *J. Am. Chem. Soc.*, 2014, **136**, 12828-12831.
- 8 (a) Y. He, S. Xiang and B. Chen, *J. Am. Chem. Soc.*, 2011, **133**, 14570-14573; (b) W. Yang, A. Greenaway, X. Lin, R. Matsuda, A. J. Blake, C. Wilson, W. Lewis, P. Hubberstey, S. Kitagawa, N. R. Champness and M. Schroder, *J. Am. Chem. Soc.*, 2010, **132**, 14457-14469; (c) H. Wang, B. Li, H. Wu, T.-L. Hu, Z. Yao, W. Zhou, S. Xiang and B. Chen, *J. Am. Chem. Soc.*, 2015, **137**, 9963-9970; (d) W. Yan, X. Yu, T. Yan, D. Wu, E. Ning, Y. Qi, Y.-F. Han, and Q. Li, *Chem. Comm.*, 2017, **53**, 3677-3680; (e) C. A. Zentner, H. W. H. Lai, J. T. Greenfield, R. A. Wiscons, M. Zeller, C. F. Campana, O. Talu, S. A. FitzGerald and J. L. C. Rowsella, *Chem. Comm.*, 2015, **51**, 11642-11645; (f) P. Li, Y. He, Y. Zhao, L. Weng, H. Wang, R. Krishna, H. Wu, W. Zhou, M. O'Keefe, Y. Han and B. Chen, *Angew. Chem. Int. Ed.*, 2015, **54**, 574-577; (g) F. Hu, C. Liu, M. Wu, J. Pang, F. Jiang, D. Yuan and M. Hong, *Angew. Chem Int. Ed.*, 2017, **56**, 2101-2104.
- 9 M. J. Zaworotko, *Chem. Soc. Rev.*, 1994, **23**, 283-288.
- 10 (a) T. Ben, H. Ren, S. Ma, D. Cao, J. Lan, X. Jing, W. Wang, J. Xu, F. Deng, J. M. Simmons, S. Qui and G. Zhu, *Angew. Chem. Int. Ed.* 2009, **48**, 9457-9460; (b) W. Lu, D. Yuan, D. Zhao, C. I. Schilling, O. Plietzsch, T. Muller, S. Bräse, J. Guenther, J. Blümel, R. Krishna, Z. Li and H.-C. Zhou, *Chem. Mater.*, 2010, **22**, 5964-5972; (c) W. Lu, D. Yuan, J. Sculley, D. Zhao, R. Krishna and H.-C. Zhou, *J. Am. Chem. Soc.*, 2011, **133**, 18126-18129; (d) P. Pandey, O. K. Farha, A. M. Spokoyny, C. A. Mirkin, M. G. Kanatzidis, J. T. Hupp and S. T. Nguyen, *J. Mater. Chem.*, 2011, **21**, 1700-1703; (e) S. S. Han, H. Furukawa, O. M. Yaghi and W. A. Goddard, *J. Am. Chem. Soc.*, 2008, **130**, 11580-11581; (f) H. Furukawa and O. M. Yaghi, *J. Am. Chem. Soc.*, 2009, **131**, 8875-8883.
- 11 (a) N. Malek, T. Maris, M. Simard and J. D. Wuest, *Acta Cryst.*, 2005, **E61**, o518-p520; (b) J. B. Lambert, Y. Zhao and C. L. Stern, *J. Phys. Org. Chem.*, 1997, **10**, 229-232.
- 12 (a) H. Furukawa, F. Gandara, Y.-B. Zhang, J. Jiang, W. L. Queen, M. R. Hudson and O. M. Yaghi, *J. Am. Chem. Soc.*, 2014, **136**, 4369-4381; (b) M. Almäši, V. Zelenák, A. Zukal, J. Kuchára and J. Čejka, *Dalt. Trans.*, 2016, **45**, 1233-1242; (c) Y. E. Cheon and M. P. Suh, *Chem. Commun.*, 2009, 2296-2298.
- 13 (a) R. K. Harris, P. Jackson, L. H. Merwin, B. J. Say, G. Hagele, *J. Chem. Soc., Faraday Trans. 1*, 1988, **84**, 3649-3672; (b) D. Ajami, P. M. Tolstoy, H. Dube, S. Odermatt, B. Koepe, J. Guo, H.-H. Limbach and J. Rebek, Jr. *Angew. Chem. Int. Ed.*, 2011, **50**, 528-531; (c) S. Brown, *Solid State Nucl. Magn. Res.*, 2012, **41**, 1-27; (d) X. Yuan, T.-X. Xiang, B. D. Anderson and E. Munson, *Mol. Pharmaceutics* 2015, **12**, 4518-4528.
- 14 K. Sumida, D. L. Rogow, J. A. Mason, T. M. McDonald, E. D. Bloch, Z. R. Herm, T.-H. Bae and J. R. Long, *Chem. Rev.*, 2012, **112**, 724-781.
- 15 (a) Y. Zeng, R. Zou and Y. Zhao, *Adv. Mater.* 2016, **28**, 2855-2873; (b) S. Bracco, D. Piga, I. Bassanetti, J. Perego, A. Comotti and P. Sozzani, *J. Mater. Chem A*, 2017, **5**, 10328-10337; (c) W. Lu, D. Yuan, J. Sculley, D. Zhao, R. Krishna and H.-C. Zhou, *J. Am. Chem. Soc.*, 2011, **133**, 18126-18129.
- 16 S. Galli, A. Maspero, C. Giacobbe, G. Palmisano, L. Nardo, A. Comotti, I. Bassanetti, P. Sozzani and N. Masciocchi, *J. Mater. Chem. A*, 2014, **2**, 12208-12221.
- 17 C. Bezuidenhout, P. M. Bhatt, C. Esterhuysen and L. J. Barbour, *Angew. Chem. Int. Ed.*, 2015, **54**, 2079-2083.
- 18 A. Comotti, S. Bracco, L. Ferretti and P. Sozzani, *J. Am. Chem. Soc.*, 2011, **133**, 8982-8994.
- 19 Y. He, W. Zhou, G. Qian and B. Chen, *Chem. Soc. Rev.*, 2014, **43**, 5657-5678.
- 20 (a) A. Kovacs, J. Cz. Dobrowolski, S. Ostrowski and J. E. Rode, *Int. J. Quantum Chem.*, 2017, **117**, e25358; (b) D. E. Freeman, K. Yoshino and Y. Tanaka, *J. Chem. Phys.*, 1974, **61**, 4880-4889.
- 21 (a) P. Sozzani, A. Comotti, R. Simonutti, T. Meersmann, J. W. Loga and A. Pines, *Angew. Chem. Int. Ed.*, 2000, **39**, 2695-2699; (b) A. Comotti, S. Bracco, L. Ferretti, M. Mauri, R. Simonutti and P. Sozzani, *Chem. Commun.*, 2007, 350-352; (c) A. Comotti, S. Bracco, P. Sozzani, S. Horike, R. Matsuda, J. Chen, M. Takata, Y. Kubota and S. Kitagawa, *S. J. Am. Chem. Soc.*, 2008, **130**, 13664-13672.
- 22 Loading is above 85 % of the maximum adsorbed value already at a pressure higher than 150 mmHg as shown by the isotherm at 195K.
- 23 (a) V. Kukla, J. Kornatowski, D. Demuth, I. Girnus, H. Pfeifer, L. V. C. Rees, S. Schunk, K. K. Unger and J. Karger, *Science*, 1996, **272**, 702-704; (b) T. Meersmann, J. W. Logan, R. Simonutti, S. Caldarelli, A. Comotti, P. Sozzani, L. G. Kaiser and A. Pines, *J. Phys. Chem. A*, 2000, **104**, 11665-11670.